Multichannel Distribution and Transformation of Entangled Photons with Dielectric Metasurfaces

Ya-Jun Gao,[1,‡] Zheng Wang,[1,‡] Yue Jiang,[1,‡] Ru-Wen Peng,[1,*] Zi-Yu Wang,[1] Dong-Xiang Qi,[1] Ren-Hao Fan,[1] Wen-Jie Tang,[1] and Mu Wang[1,2,†]

[1]*National Laboratory of Solid State Microstructures, School of Physics, and Collaborative Innovation Center of Advanced Microstructures, Nanjing University, Nanjing 210093, China*

[2]*American Physical Society, Ridge, New York 11961, USA*

(Received 21 December 2021; accepted 8 June 2022; published 6 July 2022)

Photonic quantum information processing relies on operating the quantum state of photons, which usually involves bulky optical components unfavorable for system miniaturization and integration. Here, we report on the transformation and distribution of polarization-entangled photon pairs with multichannel dielectric metasurfaces. The entangled photon pairs interact with metasurface building blocks, where the geometrical-scaling-induced phase gradients are imposed, and are transformed into two-photon entangled states with the desired polarization. Two metasurfaces, each simultaneously distributing polarization-entangled photons to spatially separated multiple channels M (N), may accomplish $M \times N$ channels of entanglement distribution and transformation. Experimentally we demonstrate 2×2 and 4×4 distributed entanglement states, including Bell states and superposition of Bell states, with high fidelity and strong polarization correlation. We expect this approach paves the way for future integration of quantum information networks.

DOI: 10.1103/PhysRevLett.129.023601

In quantum optics, the entanglement of photons can be achieved via polarization [1], optical paths [2], orbital angular momentum [3], or frequency mode [4]. Since polarization is convenient to detect and manipulate, polarization entanglement has been extensively studied [5,6]. Four maximally entangled states (Bell states) form a complete entangled basis of the two-photon Hilbert space and enable quantum dense coding [7], quantum cryptography [8], and quantum teleportation [9]. The superposition of Bell states can be applied for quantum process tomography [10] and quantum secret sharing [11,12]. Currently, two factors curtail the applicability of entanglement-based quantum communication. One is the loss in distributing entangled photon pairs over a long distance [8,13,14]. The other is establishing a compact quantum network for multiparty communication [13,15,16]. So far, a few network configurations have been proposed [17–19], where a polarization-entangled photon pair is usually realized via spontaneous parametric down-conversion with nonlinear crystals [20] or spontaneous four-wave mixing in silicon waveguides and fibers [21]. Meanwhile, the entanglement distribution depends on beam splitters [22], optical switches [23], and wavelength-division multiplexing [24,25]. To miniaturize the entanglement distributor, waveguide grating was introduced [19]. However, the entangled state assigned to each user is always identical to that of the photon source. Therefore, each user has to transform the distributed state into the desired one with extra wave plates. For example, when a photon pair is applied for quantum teleportation, the required state is one of four Bell states $[\psi^{\pm} = (|HV\rangle \pm |VH\rangle)/\sqrt{2},\ \phi^{\pm} = (|HH\rangle \pm |VV\rangle)/\sqrt{2}]$ [9]; when the photon pair is used for quantum secret sharing, however, the required state becomes a nonmaximally entangled state [12]. To achieve the appropriate state for specific applications, the number of wave plates increases with the number of users, making it formidable to miniaturize the quantum network.

The metasurfaces may resolve this challenge [26,27]. By modulating the phase distribution among nanoresonators in the metasurface, the amplitude, phase, polarization, and propagation direction of light [28–38] can be efficiently tuned. With the outstanding light manipulation capability, the metasurface is becoming an essential component in quantum optics [39–45]. For example, rotating each nanoresonator leads to the entanglement between the spin and orbital angular momentum of photons [39]. An array of metalenses realizes a path-encoded quantum entanglement photon source [43]. In Ref. [40], the metasurface consists of three interleaved parts. By modulating the geometrical size and rotation angle of the resonators, each part serves as the polarization beam splitter realizing multiphoton interference and state reconstruction. When the incident entangled photon pair interacts with the metasurface, the output state is projected onto different polarization bases, and the

 © 2022 American Physical Society

polarization entanglement vanishes. So far, simultaneous entanglement distribution and state transformation with metasurfaces, which are crucial in constructing integrated quantum networks, remain challenging.

This Letter presents a new strategy to realize entanglement distribution and transformation with two metasurfaces. Each metasurface comprises silicon nanoresonators with a gradient of geometrical-scaling-induced (GSI) phase [33,38] and has multiple output channels. By judiciously designing the resonators in the unit cell, we can simultaneously realize entanglement distribution and transformation of two-photon quantum states. To prove this concept, we experimentally demonstrate 2×2 and 4×4 entanglement distributors. This approach significantly reduces the number of conventional optical components in a quantum network.

Figure 1 illustrates the basic principle. The spontaneous parametric down-conversion light source generates polarization-entangled photon pairs $\psi^+ = (|HV\rangle + |VH\rangle)/\sqrt{2}$. The entangled photon pairs are then spatially separated, and each photon passes through one of the metasurfaces MS1 and MS2, where MS1 has M output channels $\alpha_1, \alpha_2 \ldots \alpha_M$, and MS2 has N output channels $\beta_1, \beta_2 \ldots \beta_N$. Each channel of MS1 and MS2 may form a channel pair $\mathrm{CH}_{\alpha_m,\beta_n}$ $(m = 1, 2, \ldots M,\ n = 1, 2, \ldots N)$. By elaborately designing the resonators in the unit cell, we can distribute the entangled photons to each channel pair behind the metasurfaces. Meanwhile, the entangled state is transformed from the original ψ^+ to different forms, such as $\psi^- = (|HV\rangle - |VH\rangle)/\sqrt{2}$, $\phi^+ = (|HH\rangle + |VV\rangle)/\sqrt{2}$, $\phi^- = (|HH\rangle - |VV\rangle)/\sqrt{2}$, or the superposition of these Bell states.

When the photon beam shines on a metasurface, each resonator in the unit cell scatters with a specific phase modulation determined by its physical features. The interference of the scattering from the resonators can be described by the Jones matrix [27]. We treat each diffraction beam in a specific order as an output channel. When each photon of the entangled photon pair ψ^+ passes through a metasurface, the probability of the photon coming out from a particular output channel equals the classical diffraction efficiency [46]. The output state distributing to the α_m channel of MS1 combined with the β_n channel of MS2 has the form

$$|\Psi_{m,n}\rangle = \frac{1}{\sqrt{2}}(J_{m,\mathrm{MS1}}|H\rangle J_{n,\mathrm{MS2}}|V\rangle + J_{m,\mathrm{MS1}}|V\rangle J_{n,\mathrm{MS2}}|H\rangle), \quad (1)$$

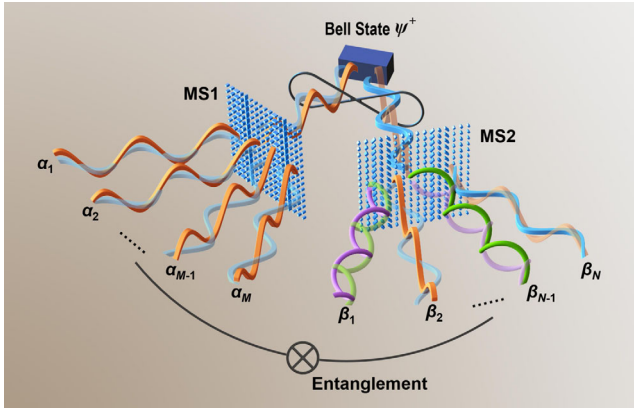

FIG. 1. The schematic of the quantum entanglement distribution and transformation via two metasurfaces composed of silicon nanoresonators with GSI phase. The polarization-entangled photon pairs with the state of $\psi^+ = (|HV\rangle + |VH\rangle)/\sqrt{2}$ are generated from the light source. The photon pairs are spatially separated, and each photon passes through either MS1 (with M output channels) or MS2 (with N output channels). Two channels from MS1 and MS2, respectively, form a channel pair. Behind metasurfaces, the entangled state distributing to each channel pair appears either in the Bell state or in the superposition of Bell states. The orange (blue) wave represents $|V\rangle$ ($|H\rangle$) state of the single photon and the purple (green) wave represents the left-handed (right-handed) circularly polarized state. Each color has bright and dimmed shades, illustrating the polarization-correlated entangled photon pair. At the input side, the spatially separated entangled photons possess the same shade. Similarly, at the output end, the entangled photons distributing to the channel α_m $(m = 1, 2, \ldots M)$ of MS1 and channel β_n $(n = 1, 2, \ldots N)$ of MS2 possess the same shade.

where $J_{m,\mathrm{MS1}}$ ($J_{n,\mathrm{MS2}}$) is the Jones matrix describing the physical response of the α_m (β_n) channel of MS1 (MS2).

The metasurface made of cuboid silicon resonators transforms the input state. The geometrical parameters of the resonators contribute the GSI phase ϕ_s and $\phi_s + \Delta\phi_s$ [33], which denotes the phase added by the resonator when the normal incidence is polarized along the long (short) principal axis of the resonator, respectively. The unit cell of our metasurface consists of eight resonators with the same rotation angle and height but different lengths and widths. Each satisfies $\Delta\phi_s$ equaling $\pi/2$ or $-\pi/2$, and ϕ_s is elaborately designed to achieve a specific GSI phase for transforming the input state [47]. Here, $s = 1, 2 \ldots 8$. The concrete form of $J_{m,\mathrm{MS1}}$ is

$$J_{m,\mathrm{MS1}} = R(-\theta_{\mathrm{MS1}}) \times \begin{bmatrix} C_m \sum_{s=1}^{8} e^{-i\frac{2\pi s D_m}{8}} e^{i\phi_s} & 0 \\ 0 & C_m \sum_{s=1}^{8} e^{-i\frac{2\pi s D_m}{8}} e^{i(\phi_s+\Delta\phi_s)} \end{bmatrix} \times R(\theta_{\mathrm{MS1}}), \quad (2)$$

where D_m is the diffraction order of the α_m channel of MS1, C_m is a parameter related to the transmittance of the resonator, wavelength, and periodicity in the x direction. θ_{MS1} is the rotation angle of the resonator from the x axis, and $R(\theta_{\mathrm{MS1}})$ is the rotation matrix with the form $R(\theta_{\mathrm{MS1}}) = \left[\begin{smallmatrix} \cos\theta_{\mathrm{MS1}} & \sin\theta_{\mathrm{MS1}} \\ -\sin\theta_{\mathrm{MS1}} & \cos\theta_{\mathrm{MS1}} \end{smallmatrix}\right]$. The specific form of $J_{n,\mathrm{MS2}}$ is similar to $J_{m,\mathrm{MS1}}$, with D_n representing the diffraction order of the β_n channel of MS2. Equation (2) satisfies the general form of the wave plate $R\tilde{J}_m R$, where $\tilde{J}_m$ is the diagonal matrix, and R is the rotation matrix. In this operation, the detailed output state is determined by the enantiomorphism, size, spatial sequence, and the separation of resonators in the unit cell [33,38].

According to Eq. (1), to transform the original state $\psi^+ = (|HV\rangle + |VH\rangle)/\sqrt{2}$ to another state, such as $(|HV\rangle - |VH\rangle)/\sqrt{2}$ or $(|HH\rangle + i|VV\rangle)/\sqrt{2}$, the output channel of the metasurface should act as a half wave plate (HWP) or a quarter wave plate (QWP). To fulfill such requirements, we select resonators in the unit cell from a pool of 16 building blocks of different sizes [47], following a method to iterate over all combinations of the resonators from the pool to identify the optimal unit cell that functions as the desired wave plate for each diffraction channel [33,38].

Figure 2(a) illustrates the schematic of the experimental setup. The periodically poled $KTiOPO_4$ (PPKTP) crystal in a Sagnac interferometer generates polarization-entangled photon pairs at 810 nm via the spontaneous parametric down-conversion process. Then the down-converted photon pairs pumped by two counterpropagating beams are spatially separated, and each photon passes through one metasurface [47]. The QWP and HWP are placed in front of the metasurface to generate the desired input entangled state. When the input Bell state is ψ^+, the fast axis of both wave plates is set to 0°. To verify the polarization-entanglement state distributed to each channel pair, we measure quantum state tomography (QST), S parameter, and two-photon polarization interference fringes [47]. We reconstruct the density matrix using the maximum likelihood estimation method [57] based on 16 measured two-photon coincidence counts by rotating the QWP and HWP behind MS1 and MS2. The fidelity is defined as $F(\rho,\tilde{\rho}) = [\mathrm{Tr}(\sqrt{\tilde{\rho}^{1/2}\rho\tilde{\rho}^{1/2}})]^2$, where $\tilde{\rho}$ is the reconstructed density matrix, and ρ is the density matrix of the expected entangled state. The near-unity fidelity indicates that the entangled state is closer to the desired state. Further, the S parameter is measured according to [58]. To violate the Clauser-Horne-Shimony-Holt (CHSH) inequality, the absolute value of the S parameter should be larger than 2, which signifies the entanglement of the quantum state [58]. In measuring the two-photon polarization interference fringes [20], the rotation angle of the fast axis of the HWP behind MS1 is fixed at 0° and 22.5° to project photon in this path onto the horizontally polarized ($|H\rangle$) and right-handed circularly polarized ($|R\rangle$) states, respectively. The two-photon coincidence count is measured by tuning the HWP angle behind MS2. The interference visibility is defined as $V = [(c_{\max} - c_{\min})/(c_{\max} + c_{\min})]$, where $c_{\max}$ and $c_{\min}$ are the maximum and minimum of the measured coincidence counts [20]. The theoretical bound to violate Bell's inequality is that the interference visibility exceeds 71% for each curve, indicating the occurrence of the quantum state entanglement [42,58].

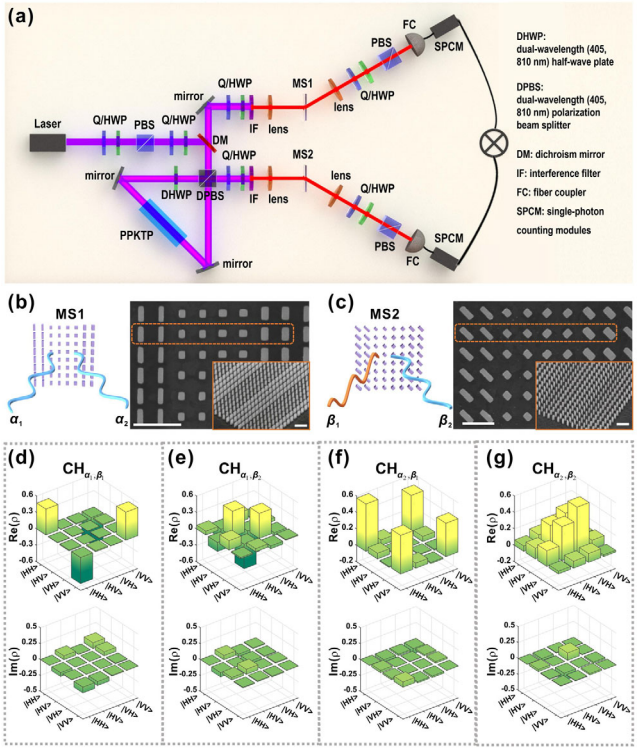

FIG. 2. (a) Schematics of the experimental setup, consisting of parts of photon-pair generation, entanglement distribution and transformation via metasurfaces, and quantum state tomography. (b),(c) SEM micrographs of the fabricated metasurfaces, MS1 and MS2. MS1 outputs channels α_1 and α_2. MS2 outputs channels β_1 and β_2. The dashed line box marks the unit cell. The inset is the oblique view of the fabricated sample. The white bars represent 1 μm. The schematic of the output state when a single photon horizontally polarized passes through the metasurface is illustrated on the left. (d)–(g) The reconstructed density matrices (the real and imaginary part) of the entangled states distributed to four channel pairs with QST measurements.

The structures of MS1 and MS2 are illustrated in Figs. 2(b) and 2(c), respectively. The rotation angle of resonators in MS1 is zero ($\theta_{\mathrm{MS1}} = 0$), while in MS2 it keeps 45° ($\theta_{\mathrm{MS2}} = 45°$). From Eq. (2), MS1 has two output channels α_1 and α_2. Similarly, MS2 has two output channels, β_1 and β_2. Detailed structural parameters are presented in [47]. We obtain the output state at each channel pair by taking the specific form of $J_{m,\mathrm{MS1}}$ and $J_{n,\mathrm{MS2}}$ into Eq. (1), with $m(n) = 1, 2$. The expected states are

$\phi^- = (|HH\rangle - |VV\rangle)/\sqrt{2}$ (at CH_{α_1,β_1}), $\psi^- = (|HV\rangle - |VH\rangle)/\sqrt{2}$ (at CH_{α_1,β_2}), $\phi^+ = (|HH\rangle + |VV\rangle)/\sqrt{2}$ (at CH_{α_2,β_1}), and $\psi^+ = (|HV\rangle + |VH\rangle)/\sqrt{2}$ (at CH_{α_2,β_2}), respectively. In this way, four Bell states are distributed to four different channel pairs. To verify the quantum entanglement, we reconstruct the quantum state with the QST measurements with the setup in Fig. 2(a). The reconstructed density matrices of four-channel pairs are illustrated in Figs. 2(d)–2(g). The fidelities between the reconstructed and ideal entangled state of CH_{α_1,β_1}, CH_{α_1,β_2}, CH_{α_2,β_1}, and CH_{α_2,β_2} are 0.9673 ± 0.0024, 0.9065 ± 0.0049, 0.9598 ± 0.0029, and 0.8703 ± 0.0075, respectively. Four density matrices agree with the matrices of the ideal states ϕ^-, ψ^-, ϕ^+, and ψ^+. Measurements of the S parameter and two-photon polarization interference fringes are illustrated in [47]. The S parameters are above 2, and the interference visibilities are above 71%. These data confirm that four Bell states are generated in four different channel pairs.

We can obtain an arbitrary entangled state at the specific output channel pair by designing the resonators in the unit cell. Meanwhile, the number of channels can be accurately controlled by the spatial period of the unit cell and the structural parameters of each resonator [33,38]. Figure 3 shows an example where MS1 and MS2 each have four output channels denoted as α_1, α_2, α_3, α_4 and β_1, β_2, β_3, β_4. There are a total of 16 (4×4) channel pairs. The unit cells of MS1 and MS2 are redesigned accordingly [Figs. 3(a) and 3(b)]. The rotation angle of resonators in MS1 is zero, whereas that in MS2 keeps 45°. By taking the concrete form of $J_{m,MS1}$ and $J_{n,MS2}$ in Eq. (1), we obtain 16 entangled states: four Bell states, eight superpositions of the two Bell states, and four superpositions of all Bell states [47]. With the QST measurements, we reconstruct the 16 quantum states. The reconstructed density matrices of four output states $|\Psi_{3,2}\rangle = \phi^+ + i\phi^-$, $|\Psi_{3,3}\rangle = \phi^+ + i\phi^- - i\psi^+ - \psi^-$, $|\Psi_{4,2}\rangle = \phi^+$, and $|\Psi_{4,3}\rangle = \phi^+ - i\psi^+$ are shown in Figs. 3(c)–3(f), and the rest 12 states are provided in [47]. Figure 4(a) shows the fidelities of the 16 states. Most values are above 0.880, with the median at 0.892 ± 0.017. The results confirm the polarization-entanglement distribution to any channel pair of the two metasurfaces.

Further, the CHSH inequality has been tested, and the S parameters of all channel pairs are provided in Fig. 4(b). The S parameters of 14 pairs are above 2, indicating the violation of CHSH inequality in these channel pairs. We also measure the two-photon polarization interference fringes. Figures 4(c)–4(f) are the two-photon coincidence counts measured in 20 s at CH_{α_3,β_2}, CH_{α_3,β_3}, CH_{α_4,β_2}, and CH_{α_4,β_3} as a function of the HWP angle placed behind MS2. The HWP angle placed behind MS1 is fixed at 0° (the dark line) and 22.5° (the red line). For each channel pair, the

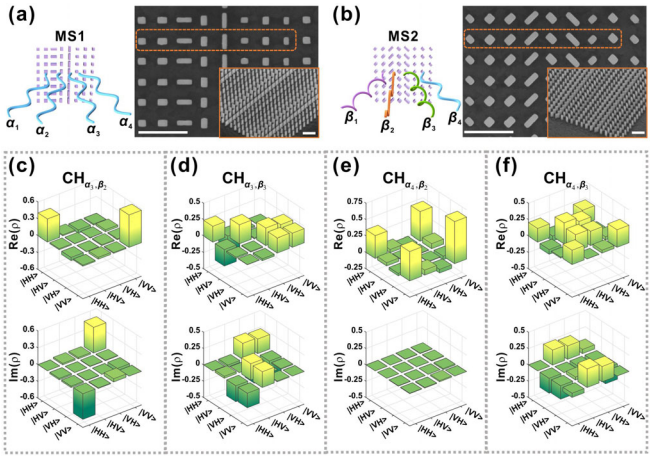

FIG. 3. (a),(b) SEM micrographs of the fabricated metasurfaces, MS1 and MS2. MS1 outputs four channels α_1, α_2, α_3, and α_4. MS2 outputs four channels β_1, β_2, β_3, and β_4. The dashed line box marks the unit cell. The inset is the oblique view of the fabricated sample. The white bars all represent 1 μm. The schematic of the output state when a single photon horizontally polarized passes through the metasurface is illustrated on the left. (c)–(f) The reconstructed density matrices (the real and imaginary part) of the entangled states distributed to 4 among 16 channel pairs with QST measurements.

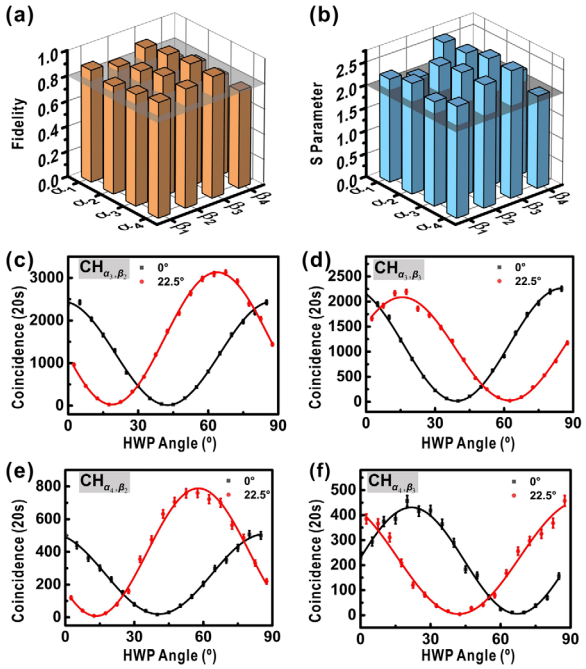

FIG. 4. (a) The fidelities of the 16 states generated by the metasurfaces in Fig. 3 based on the QST measurement. (b) S parameters of the entangled states distributed to the 16 channel pairs. (c)–(f) The two-photon coincidence counts measured in 20 s at channel pair CH_{α_3,β_2}, CH_{α_3,β_3}, CH_{α_4,β_2}, and CH_{α_4,β_3} as a function of the HWP angle placed behind MS2. The error bar is plotted assuming that the coincidence counts satisfy Poissonian photon statistics [46], which is the standard deviation of the count value of Ω ($\sqrt{\Omega}$).

measured interference visibilities in percentage are (98.85 ± 0.31) [98.23 ± 0.33], (98.53 ± 0.36) [97.38 ± 0.49], (92.62 ± 1.64) [97.95 ± 0.72], and (97.49 ± 1.07) [97.94 ± 0.94], respectively. The visibilities in the round and square brackets are measured when the fast axis of the HWP behind MS1 is rotated to 0° and 22.5°, respectively. Both visibilities are well above 71% for each channel pair, confirming the strong polarization correlation of the photon pair and the violation of Bell's inequality. These results are consistent with the S parameters measurement. The two-photon polarization interference fringes of all channel pairs are plotted in [47]. The measurements of QST, S parameter, and two-photon polarization interference fringes confirm that polarization-entanglement distribution and transformation have indeed been realized in 16 channel pairs.

It is noteworthy that when the resonator sequence is determined, the resonator rotation angle determines the distributed entangled state. Let us consider the sequence in Fig. 2. Assume that the rotation angle of resonators in MS1 (MS2) is θ_1 (θ_2). Then the rotation angle determines $|\Psi_{m,n}\rangle$ [Eq. (1)]. For example, when θ_1 and θ_2 are set as 0 and $\pi/4$, respectively, the four output states distributed to $\mathrm{CH}_{\alpha_m,\beta_n}$ [with $m(n) = 1,\ 2$] are four different Bell states. If, however, both θ_1 and θ_2 are set as 0, the entangled states at $\mathrm{CH}_{\alpha_1,\beta_2}$ and $\mathrm{CH}_{\alpha_2,\beta_1}$ are ψ^-, and the entangled states at $\mathrm{CH}_{\alpha_1,\beta_1}$ and $\mathrm{CH}_{\alpha_2,\beta_2}$ are ψ^+. If θ_1 and θ_2 are both set as $\pi/4$, the entangled states at $\mathrm{CH}_{\alpha_1,\beta_1}$ and $\mathrm{CH}_{\alpha_2,\beta_2}$ remain ψ^+, whereas those distributed to $\mathrm{CH}_{\alpha_1,\beta_2}$ and $\mathrm{CH}_{\alpha_2,\beta_1}$ become ϕ^+. Therefore, the entangled state distributing to a specific channel pair depends on the rotation angle of the resonators in the unit cell of the metasurface, in addition to their enantiomorphism and sequence.

The strategy proposed here can be applied to integrated quantum networking. Suppose each user is distributed to one channel, and the metasurfaces construct a network consisting of $M \times N$ users. With the distributed entangled photon pairs, $M \times N$ user pairs can independently implement quantum key distribution protocols BBM92 [8,59], E91 [60], or BKM07 [61], quantum teleportation [9], and quantum dense coding [1]. A detailed description of the entangled quantum key distribution based on the BBM92 protocol is given in [47].

To summarize, we demonstrate an approach for integrated entanglement distribution and transformation based on GSI metasurfaces. The experimental realization of 2×2 and 4×4 entanglement distributors indicates that GSI metasurfaces are suitable for distributing different photon states to a large number of users. This strategy significantly decreases the number of conventional optical components in constructing a quantum network. It is a hallmark development in the miniaturization and integration of optical quantum networks. It should be enlightening to transform quantum entanglement, build quantum networks, and develop on-chip quantum information processing.

The authors acknowledge financial support from the National Key R&D Program of China (No. 2017YFA0303702, No. 2020YFA0211300) and the National Natural Science Foundation of China (Grants No. 11634005, No. 11974177, and No. 61975078).

*Corresponding author.
rwpeng@nju.edu.cn
†Corresponding author.
muwang@nju.edu.cn
‡These authors contributed equally to this work.

[1] X.-M. Hu, Y. Guo, B.-H. Liu, Y.-F. Huang, C.-F. Li, and G.-C. Guo, Sci. Adv. **4**, eaat9304 (2018).
[2] X-Y. Xu, W.-W. Pan, Q.-Q. Wang, J. Dziewior, L. Knips, Y. Kedem, K. Sun, J.-S. Xu, Y.-J. Han, C.-F. Li, G.-C. Guo, and L. Vaidman, Phys. Rev. Lett. **122**, 100405 (2019).
[3] M. Erhard, M. Malik, M. Krenn, and A. Zeilinger, Nat. Photonics **12**, 759 (2018).
[4] L. Y. Qu, J. Cotler, F. Ma, J.-Y. Guan, M.-Y. Zheng, X. Xie, Y.-A. Chen, Q. Zhang, F. Wilczek, and J.-W. Pan, Phys. Rev. Lett. **123**, 243601 (2019).
[5] W. A. T. Nogueira, S. P. Walborn, S. Pádua, and C. H. Monken, Phys. Rev. Lett. **92**, 043602 (2004).
[6] T.-C. Wei, J. B. Altepeter, D. Branning, P. M. Goldbart, D. F. V. James, E. Jeffrey, P. G. Kwiat, S. Mukhopadhyay, and N. A. Peters, Phys. Rev. A **71**, 032329 (2005).
[7] B. P. Williams, R. J. Sadlier, and T. S. Humble, Phys. Rev. Lett. **118**, 050501 (2017).
[8] J. Yin *et al.*, Nature (London) **582**, 501 (2020).
[9] D. Bouwmeester, J. W. Pan, K. Mattle, M. Eibl, H. Weinfurter, and A. Zeilinger, Nature (London) **390**, 575 (1997).
[10] J. B. Altepeter, D. Branning, E. Jeffrey, T. C. Wei, P. G. Kwiat, R. T. Thew, J. L. O'Brien, M. A. Nielsen, and A. G. White, Phys. Rev. Lett. **90**, 193601 (2003).
[11] A. G. White, D. F. V. James, P. H. Eberhard, and P. G. Kwiat, Phys. Rev. Lett. **83**, 3103 (1999).
[12] B. P. Williams, J. M. Lukens, N. A. Peters, B. Qi, and W. P. Grice, Phys. Rev. A **99**, 062311 (2019).
[13] H.-K. Lo, M. Curty, and K. Tamaki, Nat. Photonics **8**, 595 (2014).
[14] S. Wengerowsky, S. K. Joshi, F. Steinlechner, J. R. Zichi, S. M. Dobrovolskiy, R. van der Molen, J. W. N. Los, V. Zwiller, M. A. M. Versteegh, A. Mura, D. Calonico, M. Inguscio, H. Hübel, L. Bo, T. Scheidl, A. Zeilinger, A. Xuereb, and R. Ursin, Proc. Natl. Acad. Sci. U.S.A. **116**, 6684 (2019).
[15] C. Simon, Nat. Photonics **11**, 678 (2017).
[16] A. Acín, I. Bloch, H. Buhrman, T. Calarco, C. Eichler, J. Eisert, D. Esteve, N. Gisin, S. J. Glaser, F. Jelezko, S. Kuhr, M. Lewenstein, M. F. Riedel, P. O. Schmidt, R. Thew, A. Wallraff, I. Walmsley, and F. K Wilhelm, New J. Phys. **20**, 080201 (2018).

[17] L.-K. Chen, H.-L. Yong, P. Xu, X.-C. Yao, T. Xiang, Z.-D. Li, C. Liu, H. Lu, N.-L. Liu, L. Li, T. Yang, C.-Z. Peng, B. Zhao, Y.-A. Chen, and J.-W. Pan, Nat. Photonics **11**, 695 (2017).

[18] D. Stucki *et al.*, New J. Phys. **13**, 123001 (2011).

[19] P. D. Kumavor, A. C. Beal, S. Yelin, E. Donkor, and B. C. Wang, J. Lightwave Technol. **23**, 268 (2005).

[20] P. G. Kwiat, K. Mattle, H. Weinfurter, A. Zeilinger, A. V. Sergienko, and Y. Shih, Phys. Rev. Lett. **75**, 4337 (1995).

[21] X. Li, P. L. Voss, J. E. Sharping, and P. Kumar, Phys. Rev. Lett. **94**, 053601 (2005).

[22] B. Fröhlich, J. F. Dynes, M. Lucamarini, A. W. Sharpe, Z. Yuan, and A. J. Shields, Nature (London) **501**, 69 (2013).

[23] T.-Y. Chen, J. Wang, H. Liang, W.-Y. Liu, Y. Liu, X. Jiang, Y. Wang, X. Wan, W.-Q. Cai, L. Ju, L.-K. Chen, L.-J. Wang, Y. Gao, K. Chen, C.-Z. Peng, Z.-B. Chen, and J.-W. Pan, Opt. Express **18**, 27217 (2010).

[24] S. Wengerowsky, S. K. Joshi, F. Steinlechner, H. Hübel, and R. Ursin, Nature (London) **564**, 225 (2018).

[25] J. Wang, F. Sciarrino, A. Laing, and M. G. Thompson, Nat. Photonics **14**, 273 (2020).

[26] N. Yu, P. Genevet, M. A. Kats, F. Aieta, J.-P. Tetienne, F. Capasso, and Z. Gaburro, Science **334**, 333 (2011).

[27] H.-T. Chen, A. J. Taylor, and N. Yu, Rep. Prog. Phys. **79**, 076401 (2016).

[28] S.-C. Jiang, X. Xiong, Y.-S. Hu, Y.-H. Hu, G.-B. Ma, R.-W. Peng, C. Sun, and M. Wang, Phys. Rev. X **4**, 021026 (2014).

[29] R.-H. Fan, Y. Zhou, X.-P. Ren, R.-W. Peng, S.-C. Jiang, D.-H. Xu, X. Xiong, X.-R. Huang, and M. Wang, Adv. Mater. **27**, 1201 (2015).

[30] A. Arbabi, Y. Horie, M. Bagheri, and A. Faraon, Nat. Nanotechnol. **10**, 937 (2015).

[31] J. P. Balthasar Mueller, N. A. Rubin, R. C. Devlin, B. Groever, and F. Capasso, Phys. Rev. Lett. **118**, 113901 (2017).

[32] A. C. Overvig, S. Shrestha, S. C. Malek, M. Lu, A. Stein, C. Zheng, and N. Yu, Light Sci. Appl. **8**, 92 (2019).

[33] Y.-J. Gao, X. Xiong, Z. Wang, F. Chen, R.-W. Peng, and M. Wang, Phys. Rev. X **10**, 031035 (2020).

[34] Q. Fan, M. Liu, C. Zhang, W. Zhu, Y. Wang, P. Lin, F. Yan, L. Chen, H. J. Lezec, Y. Lu, A. Agrawal, and T. Xu, Phys. Rev. Lett. **125**, 267402 (2020).

[35] Y. Yuan, S. Sun, Y. Chen, K. Zhang, X. Ding, B. Ratni, Q. Wu, S. N. Burokur, and C.-W. Qiu, Adv. Sci. **7**, 2001437 (2020).

[36] B. Xiong, Y. Xu, J. Wang, L. Li, L. Deng, F. Cheng, R.-W. Peng, M. Wang, and Y. Liu, Adv. Mater. **33**, 2005864 (2021).

[37] A. H. Dorrah, N. A. Rubin, A. Zaidi, M. Tamagnone, and F. Capasso, Nat. Photonics **15**, 287 (2021).

[38] Y.-J. Gao, Z. Wang, W. Tang, X. Xiong, Z. Wang, F. Chen, R.-W. Peng, and M. Wang, Phys. Rev. B **104**, 125419 (2021).

[39] T. Stav, A. Faerman, E. Maguid, D. Oren, V. Kleiner, E. Hasman, and M. Segev, Science **361**, 1101 (2018).

[40] K. Wang, J. G. Titchener, S. S. Kruk, L. Xu, H.-P. Chung, M. Parry, I. I. Kravchenko, Y.-H. Chen, A. S. Solntsev, Y. S. Kivshar, D. N. Neshev, and A. A. Sukhorukov, Science **361**, 1104 (2018).

[41] P. Georgi, M. Massaro, K.-H. Luo, B. Sain, N. Montaut, H. Herrmann, T. Weiss, G. Li, C. Silberhorn, and T. Zentgraf, Light Sci. Appl. **8**, 70 (2019).

[42] J. Zhou, S. Liu, H. Qian, Y. Li, H. Luo, S. Wen, Z. Zhou, G. Guo, B. Shi, and Z. Liu, Sci. Adv. **6**, eabc4385 (2020).

[43] L. Li, Z. Liu, X. Ren, S. Wang, V.-C. Su, M.-K. Chen, C. H. Chu, H. Y. Kuo, B. Liu, W. Zang, G. Guo, L. Zhang, Z. Wang, S. Zhu, and D. P. Tsai, Science **368**, 1487 (2020).

[44] Q. Li, W. Bao, Z. Nie, Y. Xia, Y. Xue, Y. Wang, S. Yang, and X. Zhang, Nat. Photonics **15**, 267 (2021).

[45] A. S. Solntsev, G. S. Agarwal, and Y. S. Kivshar, Nat. Photonics **15**, 327 (2021).

[46] M. Fox, *Quantum Optics* (Oxford University Press, New York, 2006).

[47] See Supplemental Material at http://link.aps.org/supplemental/10.1103/PhysRevLett.129.023601 for further theoretical and experimental details, which includes Refs. [48–56].

[48] N. Gisin, G. Ribordy, W. Tittel, and H. Zbinden, Rev. Mod. Phys. **74**, 145 (2002).

[49] X. Liu, X. Yao, R. Xue, H. Wang, H. Li, Z. Wang, L. You, X. Feng, F. Liu, K. Cui, Y. Huang, and W. Zhang, APL Photonics **5**, 076104 (2020).

[50] N. B. Lingaraju, H.-H. Lu, S. Seshadri, D. E. Leaird, A. M. Weiner, and J. M. Lukens, Optica **8**, 329 (2021).

[51] D. Sell, J. Yang, S. Doshay, R. Yang, and J. A. Fan, Nano Lett. **17**, 3752 (2017).

[52] J. R. Ong, H. S. Chu, V. H. Chen, A. Y. Zhu, and P. Genevet, Opt. Lett. **42**, 2639 (2017).

[53] J. Jahns, M. M. Downs, M. E. Prise, N. Streibi, and S. J. Walker, Opt. Eng. (Bellingham, Wash.) **28**, 281267 (1989).

[54] C. Zhou and L. Liu, Appl. Opt. **34**, 5961 (1995).

[55] D. Sell, J. Yang, S. Doshay, and J. A. Fan, Adv. Opt. Mater. **5**, 1700645 (2017).

[56] P. Meystre and M. Sargent, *Elements of Quantum Optics* (Springer, New York, 2007).

[57] D. F. V. James, P. G. Kwiat, W. J. Munro, and A. G. White, Phys. Rev. A **64**, 052312 (2001).

[58] J. F. Clauser and A. Shimony, Rep. Prog. Phys. **41**, 1881 (1978).

[59] C. H. Bennett, G. Brassard, and N. D. Mermin, Phys. Rev. Lett. **68**, 557 (1992).

[60] A. K. Ekert, Phys. Rev. Lett. **67**, 661 (1991).

[61] M. Boyer, D. Kenigsberg, and T. Mor, Phys. Rev. Lett. **99**, 140501 (2007).